TURBULENT GAS MIXING IN STRONG DENSITY STRATIFIED SHEAR AND NON-SHEAR FLOWS

B. Krohn[1,2*], M. Sharabi[2], B. Niceno[1,2], H.-M. Prasser[1,2]
[1]Laboratory of Nuclear Energy Systems
Institute of Energy Technology
Swiss Federal Institute of Technology, 8092 Zürich, Switzerland
krohn@lke.mavt.ethz.ch; medhat.sharabi@psi.ch; bojan.niceno@psi.ch;
prasser@lke.mavt.ethz.ch

[2]Laboratory of Thermal-Hydraulics
Nuclear Energy and Safety Research Department
Paul Scherrer Institut
5232 Villigen PSI, Switzerland

H. Bijleveld[3], A. Shams[3], F. Roelofs[3]
[3]Nuclear Services for Energy, Environment & Health,
1755 LE Petten, Netherlands
bijleveld@nrg.eu; shams@nrg.eu; roelofs@nrg.eu

ABSTRACT

Turbulent mixing in the presence of density stratifications is doubtlessly the most efficient mixing process in practice. Despite its technical relevance in fields of safety in nuclear reactors, chemical process engineering and the transport of liquefied gases, as well in the simulation of fires, the phenomenon mostly rules the dynamics in atmospheres and ocean currents.
To study the fundamental turbulent mixing phenomena in the presence of high density gradients and shear, an experimental facility was built, consisting of an open gas mixing loop supplying a mixing channel with square cross section, in which measurements are taken. Two gases with a range of density ratios from 1…1/7 flow past a horizontal splitter plate, dividing the inlet section into an upper and a lower leg. Reynolds numbers of each leg, range from 2'500 to 20'000. The density difference was created by using pure nitrogen and pure helium. The gas supply loop feeds the test section to establish isokinetic or shear flow conditions. Planar Particle Image Velocimetry is used to investigate the flow field in the developing mixing layer. In addition, Computational Fluid Dynamics analysis was performed making use of Large Eddy Simulation methods for model validation and the resulting flow fields are quantitatively compared. The results are presented in terms of turbulent statistics. An asymmetric development of the mixing layer is observed for all stratified cases, and with increased stratification we observe a production of turbulent kinetic energy (TKE) across the mixing layer from the denser stream towards the lighter gas. The strong formation of shear, due to an asymmetric development of momentum thickness, is found to produce TKE within the developing mixing layer and dominates the damping effect of buoyancy for stable stratification by approximately two orders of magnitude.

* Author to whom correspondence should be addressed.

KEYWORDS
Turbulent Mixing, High Density Ratio, Particle Image Velocimetry (PIV), Computational Fluid Dynamics (CFD).

1. INTRODUCTION

Mixing in turbulent regime is by far the most efficient mixing process that occurs in natural processes or technical applications. Its immense contribution to physical phenomena is ranging from astrophysical down to Kolmogorov scales. It influences thermonuclear fusion, governs the dynamics of supernovae, accretion disks and explosions, as mentioned by Abarzhi [1]. It dominates stellar convection, the dynamics of planetary interiors and mantle-lithosphere tectonics. It causes important effects on climate by controlling atmospheric and oceanic dynamics [2-4]. It strongly affects combustion under premixed or non-premixed inertial conditions [5-7]. It is used in a broad range of industrial applications and has major importance in designing innovative cooling systems of generation IV (GEN-IV) nuclear power plants [8]. Most of these phenomena are driven by non-equilibrium dynamics. Focusing on fluid dynamics, the fundamental process of turbulent mixing is usually influenced by velocity shear and density gradients. A wide variety of jet injection experiments were performed but compared to this large body of works, only a few planar mixing experiments exist where the effect of stratified shear flows on mixing efficiency is investigated. Nevertheless, this effect still remains unresolved and there is no consensus in the scientific community for a sufficient description of this important phenomenon.

2. EXPERIMENTAL SETUP

The experimental facility consists of an open GAs MIxing LOop (GAMILO) supplying two separated gas streams to a HOrizontal Mixing Experiment in a Rectangular channel (HOMER). These streams may consist of pure nitrogen or pure helium in one of the streams. GAMILO allows to conduct experiments for equal or unequal initial velocities (isokinetic conditions, $u_1 = u_2$ or shear layer conditions $u_1 \neq u_2$). The nominal velocity of each stream is controlled by a regulator valve which is connected to a Coriolis flow meter, which measures the mass flow rate $\dot{m}_i$ of each gas stream. The absolute pressure p_i is measured by a pressure gauge and a resistance temperature sensor measures the temperature T_i. The measured mass flow rate is continuously converted into a volumetric flow rate $\dot{V}_i$ according to the continuity equation and the ideal gas law with R_i being the specific gas constant:

$$\dot{V}_i = \frac{\dot{m}_i \cdot R_i \cdot T_i}{p_i} . \tag{1}$$

With the cross sectional area $A = 0.0018m^2$ of one leg, the nominal velocity u_i is calculated according to:

$$u_i = \dot{V}_i \cdot A . \tag{2}$$

A simplified representation of GAMILO is shown in Fig. 1. The gases enter GAMILO from gas batteries. Two heaters control the temperatures in each gas stream. The first heater is located at the inlet of GAMILO upstream the Coriolis flow meter, the second heater is located downstream the control valve and is controlled through the actual gas temperature monitored with PT-100 resistance sensors located in each gas stream close to the inlet to the conditioning section.
A simplified representation of the HOMER facility is shown in Fig. 2. The HOMER facility is a channel comprising two rectangular flow conditioning inlets and a measurement section with square cross section. the initially separated flow channels (upper and lower leg) of the conditioning section are equipped with

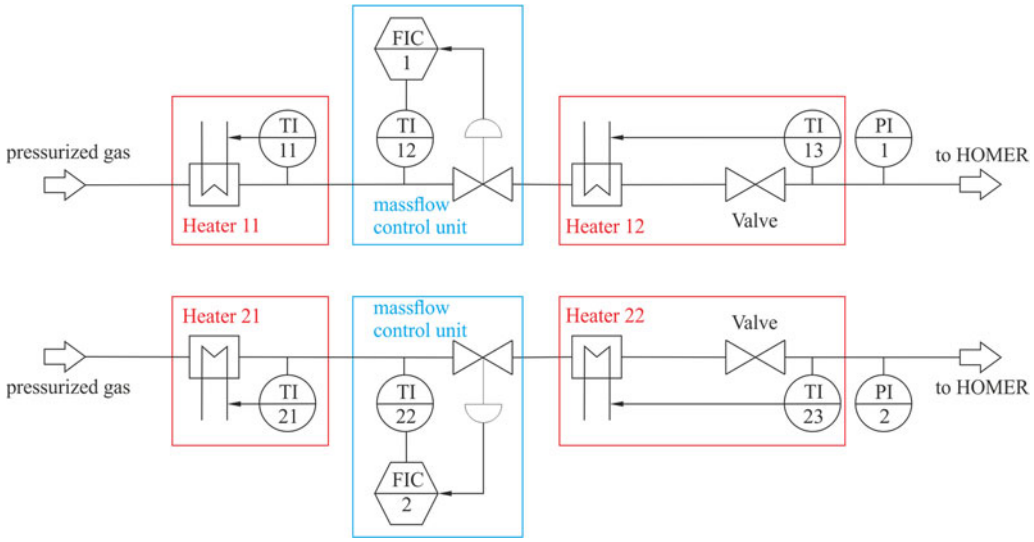

Figure 1. Simplified schematic of GAMILO.

honeycombs and grids to remove possible rotational components, introduced into the flow, by the gas supply loop and to repeatedly reduce boundary layers at each grid, thus establishing an inlet profile which is as flat and uniform as possible. The last two grids are located at $x = -100mm$ and $-250mm$ upstream the splitter plate tip. The wire diameter of each grid is $d_g = 0.4mm$ with a mesh width of $w_g = 1.6mm$.

The measurement section of the HOMER facility consists of two parts. For the first part, denoted 'position01', the field-of-view (FOV) for the velocity measurements ranges from $15 \leq x \leq 340mm$ in horizontal, and from $-25 \leq y \leq 25mm$ in vertical direction. For the second part, denoted 'position02', the FOV ranges from $475 \leq x \leq 820mm$ in horizontal, and from $-25 \leq y \leq 25mm$ in vertical direction. The temperature of each gas stream was set to $T_1 = T_2 = 30°C$. Isokinetic stably stratified mixing experiments were conducted. The nominal parameters of each test case are given in Table I. With the hydraulic diameter $d_h = 0.04m$ of a half channel, the Reynolds number Re_i is calculated. To quantify stratification strength, the Atwood number A, as a dimensionless density ratio is defined:

$$A = \frac{\rho_2 - \rho_1}{\rho_2 + \rho_1}, \tag{3}$$

where ρ_1 is the density of the lower leg and ρ_2 is the density of the upper leg. The Atwood number depicts the stratification strength of the Rayleigh-Taylor type of mixing instability for unstable stratifications. According to the convention for unstable stratifications to have positive Atwood numbers, a negative Atwood number for stable stratification is adopted.

Table I. Nominal parameters for stable stratified isokinetic mixing experiments.

$\boldsymbol{No}$	$\boldsymbol{A}$ -	$\boldsymbol{u_1 = u_2}$ m/s	$\boldsymbol{\rho_1}$ kg/m^3	$\boldsymbol{\rho_2}$ kg/m^3	$\boldsymbol{\nu_1}$ $m^2/s \cdot 10^{-5}$	$\boldsymbol{\nu_2}$ $m^2/s \cdot 10^{-5}$	$\boldsymbol{Re_1}$ -	$\boldsymbol{Re_2}$ -
T1	**0.00**	8.0	1.1116	1.1116	1.6224	1.6224	19720	19720
T2	**-0.75**	8.0	1.1116	0.1588	1.6224	12.646	19720	2530

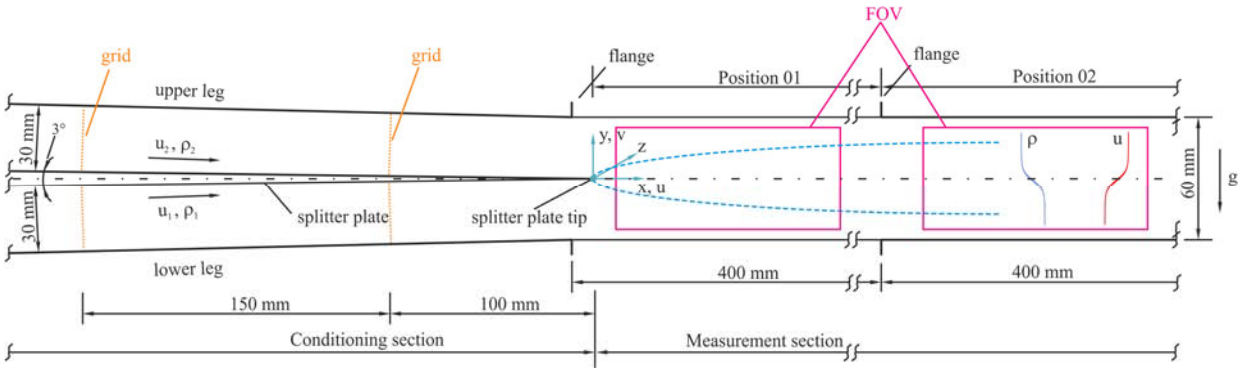

Figure 2. Simplified schematic of HOMER.

To measure the velocity field in the vertical mid-plane of the measurement section, Particle Image Velocimetry (PIV) was used. The hardware comprises a Litron NanoL laser with 200mJ and a PCO 1600 camera has a resolution of $1600 \times 1200\ pixels^2$. For each FOV (position01 and position02 in Fig. 2) one PIV recording consisting in $N = 1024$ double images recorded with a frequency of $f = 15Hz$ was conducted. For the PIV analysis with DaVis 8.2 [20] a multi pass approach with an initial interrogation window of $64 \times 64\ pixels^2$ and a final interrogation size of $12 \times 12\ pixel^2$ with 50% overlap was used. One pixel corresponds to $246 \times 246\ \mu m^2$ which results in an effective spatial resolution of $1.467 \times 1.467 mm^2$ for the velocity vectors. The time average of the velocity was calculated according to:

$$\bar{u} = \frac{1}{N}\sum_{i=1}^{N} u_i \ . \tag{4}$$

The root mean square (RMS) of velocity fluctuations was calculated using:

$$u' = \sqrt{\frac{1}{N-1}\sum_{i=1}^{N}(u_i - \bar{u})^2}\ . \tag{5}$$

Corresponding formula apply for vertical components $\bar{v}$ and v'. The components of the Reynolds stress were calculated by:

$$\tau_{xx} = u'^2, \qquad \tau_{yy} = v'^2 \text{ and } \quad \tau_{xy} = \frac{1}{N}\sum_{i=1}^{N}(u_i - \bar{u}) \cdot (v_i - \bar{v})\,. \tag{6}$$

Turbulent Kinetic Energy was calculated under the assumption that the y-component is comparable to the z-component:

$$k = {}^1\!/_2\,(u'^2 + 2 \cdot v'^2)\ . \tag{7}$$

For the order of magnitude for the statistical error estimate we refer to the method described by Bendat and Piersol [25]. Since we only know the estimate of the standard deviation (the RMS of our measurements), the confidence interval can only be constructed based on the Student's distribution, which describes the distribution of a random quantity. For a given mean value we construct the two sided uncertainty with 95% confidence level according to:

$$\left[\bar{u} - \frac{u' \cdot t_{inv}}{\sqrt{N}} \le \bar{u} < \bar{u} + \frac{u' \cdot t_{inv}}{\sqrt{N}}\right]\ , \tag{8}$$

with t_{inv} being the Student's t inverse cumulative distribution function, N the number of samples taken (in our case the number of image pairs). Since the error for the standard deviation is non-symmetric, the two sided uncertainty levels with a confidence interval of 95 %, based on the sample variance, is

estimated with X^2, the chi-squared distribution with N degrees of freedom is the distribution of a sum of the squares of N independent standard normal random variables, according to:

$$\left[\frac{(N-1)\cdot u\prime^2}{X^2} \leq u'^2 < \frac{(N-1)\cdot u\prime^2}{X^2}\right], \quad (9)$$

3. NUMERICAL METHODS

Computational Fluid Dynamics (CFD) analysis was performed making use of Large Eddy Simulation methods (LES). The following sections present the numerical methods of two groups, namely the Paul Scherrer Institute (PSI) and Nuclear Services for Energy, Environment & Health (NRG). In particular, PSI performed experiments and LES while NRG performed LES.

3.1. Numerical Methods PSI

The CFD analysis is performed with LES paradigm for model validation against the three test cases described in Table 1. The commercial software ANSYS FLUENT 14.5 [9] is used for all calculations reported in the present work. The variable properties formulation of the space-filtered Navier-Stokes equations is solved with gravity forces directly included in the momentum equations. In addition, as mixing in the channel takes place under isothermal conditions and comprises gases of different densities, a species transport equation is used to account for this process of mixing between the gases entering from the upper and lower branches of the channel. In the following subsections, details about numerical methods, computational domain and boundary conditions are discussed.

3.1.1. Computational domain and inlet boundary conditions

The adopted computational domain starts from the last grid installed in the conditioning section ($100mm$ upstream the splitter plate tip). Regarding inlet flow measurements, only the volumetric flow rate is measured in the experimental setup and there is no information available about the shape of the velocity profile or turbulent intensities prior to a distance $x = 17mm$ from the splitter plate tip where the PIV measurement system provides the flow details at the vertical mid plane. Actually, the measured velocity and turbulence profiles at $x = 17mm$ are not sufficient for imposing boundary conditions at that location considering a shorter computational domain because cross-sectional velocity profiles are required and taking into account that the velocity distribution in z-direction differs from that measured in the y-direction because of the non-square shape of the inlet sections and also because of corner effects. In addition, the mixing history is not known before that location.

A reasonable definition of inlet boundary conditions is necessary for proper comparisons of various flow development profiles along the HOMER channel and for fair validations of the adopted models. Therefore, an approach is investigated relying on trials of different velocity profile shapes at the adopted inlet location and comparing the results with the experimental data at the first location where it is available. Since LES would consume long time to perform such tests, a Reynolds-averaged Navier-Stokes (RANS) model is used instead for this purpose selecting the SST-kω turbulent model [10] because it showed reasonable results for all the simulated cases. In steady-state SST-kω based simulations, a flat and fully developed profile are imposed at the inlet sections. A fully developed profile is obtained considering a short inlet section and periodic boundary conditions. The obtained velocity profile is then used as inlet boundary condition for the real geometry. Figure 4 shows comparison of results for the test cases T1 and T2. The flat velocity profile assumption highly underestimates the velocity at $x = 17mm$, while assuming fully developed profile at the inlets overestimates the velocity predictions at that location. Therefore, a weighted velocity profile,

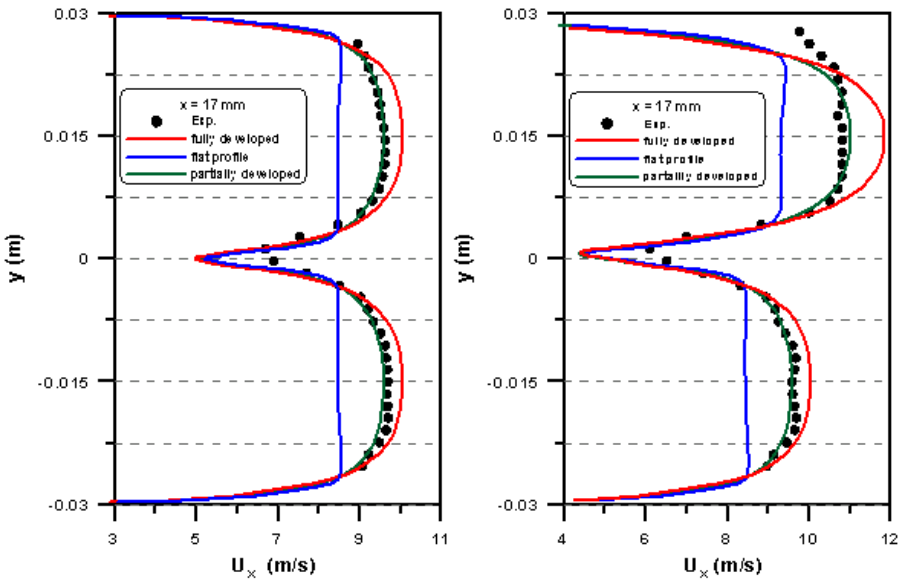

Figure 4. Comparison of the streamwise velocity profile at the location x = 17mm assuming various profile shapes at the inlet sections. (a) case T1, (b) case T2.

$$u\{x,y\} = \alpha \cdot u\{x,y\}_{developed} + (1-\alpha) \cdot u\{x,y\}_{flat}\ , \tag{10}$$

where $\alpha = 1$ corresponds to fully developed and $\alpha = 0$ corresponds to a flat velocity profile at the inlet, is tried for different values. A partially developed profile with $\alpha = 0.7$ is found to produce the best results in comparisons with experimental data as shown in Fig. 4. Although, very good agreement is obtained for the test case T1 on both sides of the channel, for the test case T2 some discrepancies are persistent close to the upper wall of the channel. The profile obtained from the experiment is flatter while the calculated one has more rounded shape. No other combination between flat and fully developed profile could produce better results. It was found that a partially developed profile with $\alpha = 0.7$ gives the best results and makes a reasonable assumption for the velocity distribution at the inlet. Sensitivity of the results on the mesh size is tested considering three meshes with different sizes of ≈ 1M, 1.5M and 2.2M (the mesh is structured with wall refinement as shown in Fig. 5). No significant difference is found when the results from the three meshes are compared.

A turbulent intensity of 3% is assumed at the inlet by making use of the level of turbulent kinetic energy measured at the location $x = 17mm$ in the turbulent core for the case T1. However, for case T2 the measured turbulent kinetic energy in the upper branch is much lower and therefore, a smaller value of 1.5% is assumed at the inlet of the upper branch for these three cases. In addition, perturbations are added to the mean velocity profile obtained from RANS simulations and applied at the specified inlet to generate time dependent inlet conditions.

3.1.3. Grids and numerical schemes for LES

A Cartesian-based mesh created by cut-cell mesh generation techniques is used for LES. The meshing procedure creates elements with aspect ratios equal to one in the three directions, which favors LES development principles. For the case including nitrogen and helium gases, the mesh size requirements for the lower and upper half of the channel are significantly different. Although the Re number at the lower half of the channel is relatively high, it is low in the upper half and it is not feasible for that half to place the first grid point inside the log layer and still have fair distribution of nodes over the small cross

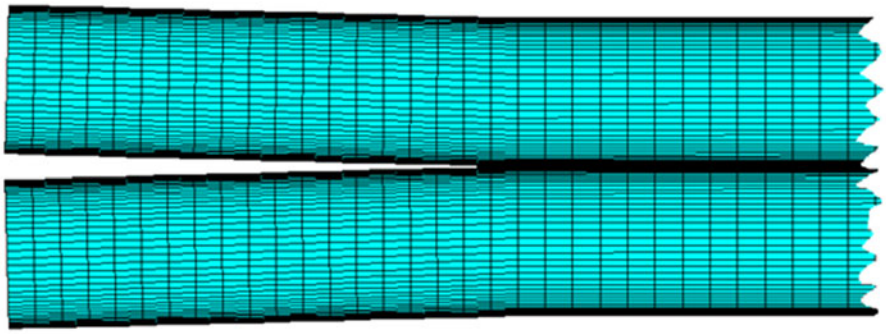

Figure 5. Cross section view of RANS mesh configurations for the HOMER test section.

section of the channel. So, a mesh that resolves the near-wall region all the way to the wall is used for all cases to have similar basis for comparison of model capabilities to reproduce the experimental data for different test cases. A prism layer is constructed along all the walls with a maximum aspect ratio of 40. The element size in the stream wise direction is restricted to mesh requirements in the transverse directions due to the cubical shape of the elements. In terms of dimensionless wall distance, the maximum grid spacing is $\Delta x^+ = \Delta y^+ = \Delta z^+ \approx 21$. At the Helium side, due to the uniformity of the grid spacing, it is even smaller and reduces to ≈ 6 for the adopted node dimensions. The first grid point is located at a distance $y^+ \approx 0.5$ and five grid points are placed in the laminar sublayer. This meshing technique eliminates the need to include unnecessary fine mesh with high aspect ratios at the middle of the channel which also affects the accuracy of numerical interpolations compared to structured mesh as illustrated in Fig. 6. In general, the grid size generated by the cut-cell method for this case is smaller than the grid generated using a structured mesh with grid spacing that fulfils the requirements for LES. A total of $\approx 7M$ grid nodes are used in the simulations.

The discretization scheme for the momentum equations is the second order accurate central difference scheme where the third-order MUSCL scheme [11] is used for discretization of convective terms in the species transport equation. For the simulated case with high density differences, the bounded central-difference scheme [9] is used instead for the momentum equations due to convergence difficulties. Implicit time integration based on second order backward differencing is used for temporal discretization with a time step of $\Delta t = 4 \times 10^{-5} s$. Pressure-velocity coupling is based on the SIMPLEC algorithm [12]. The turbulent Schmidt number (Sc) is assumed to be $Sc_t = 0.7$. The WALE sub-grid scale model [13] is used to model sub-grid stresses. This model predicts zero turbulent viscosity for laminarized regions making it more suitable for some of the cases simulated in this work. A non-iterative time step advancement is tried which reduces significantly the required CPU time, however it leads to unphysical results for the velocity field for cases with high density ratios. So, iterative advancement is adopted with reduction of residuals to $R = 1 \times 10^{-4}$.

Calculations are performed for ten flow-through residence times and flow statistics are collected only over the last five residence times, while the first five are used to reach statistically stable conditions. Extending the time window for collecting statistics did not show significant change in the results for the mean flow or RMS values.

3.2. Numerical Setup NRG

At NRG, numerical simulations of three of the experiments have been performed. In this section, the applied numerical methods are discussed.

For the simulations performed by NRG, the numerical simulations are carried out using the OpenFOAM software, version 2.2 [14] with a solver suitable for handling two different flows (twoLiquidMixingFoam). The fraction of species is solved as a passive scalar. The simulations are carried out using LES. The subgrid scale model for the LES is the local dynamic Smagorinsky model [15].

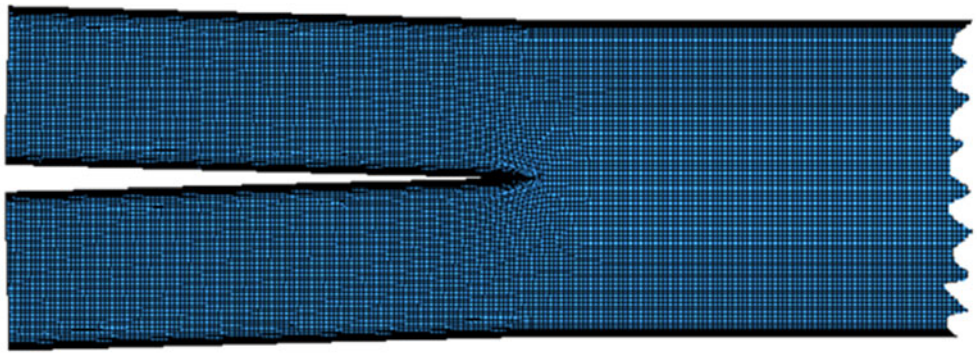

Figure 6. Cross section view of LES mesh configurations for the HOMER test section.

3.2.1. Mesh

An outline of the computational domain is given in Fig. 7. The computational domain starts $200mm$ upstream of the trailing edge of the splitter plate and ends $800mm$ downstream of it. The mixing section (downstream of the trailing edge) is $60mm$ high; the inlet channels are half of this height: $30\ mm$, see Fig. 7. The mixing section and inlet channels have a width of $60mm$ (in the direction perpendicular to the plane in Fig. 7). The height and width are corresponding to the experimental set-up. The origin of the coordinate system is at the midpoint of the trailing edge. The mesh on the walls of the splitter plate is wall resolved for the LES computations. The boundary layer is present with a cell height of $3.6 \times 10^{-5}m$ in the first cell to ensure a $y^+ \leq 1$. The boundary layer has a stretching ratio of 1.07 and contains 49 layers. The largest cells in the boundary layer have a length of $\Delta = 25$ with $\Delta = y^+(1) = 3.6 \times 10^{-5}m$.

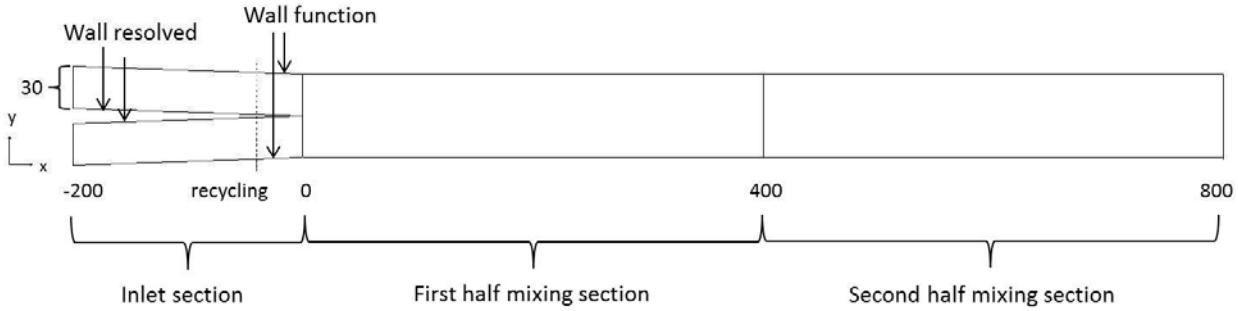

Figure 7. Outline of computational domain of the NRG simulations.

To ensure a proper capture of eddies, the boundary layer settings are also adopted in the region around the trailing edge of the splitter plate in x, y and z direction. Figure 8 displays a zoom of the mesh near the trailing edge. At the outer walls, wall function meshing is adopted and the mesh size in these cells is $\Delta = 50$ ($1.8 \times 10^{-4}\ m$). In the second half of the mixing section ($400mm < x < 800mm$, see Fig. 7), the cells are stretched in x-direction (streamwise direction) with a Stretching Ratio of $SR = 1.1$ from $\Delta = 25\ to\ \Delta = 50$. By applying all these settings, the computational mesh contains a total $17\ M$ grid points. This mesh is applied in the three cases that have been simulated. At the walls of the splitter plate a no-slip boundary condition is applied. At the outer walls of the channel a ν-SGS wall function [16] is applied. At the outlet a fixed pressure of zero Pa and a zero gradient for the velocity is applied as boundary condition. At the inlets the velocity of $0.16m/s$ downstream is mapped. The average value is set to the inlet velocities given in Table I. The fraction of species α is set to one in the upper inlet and to zero in the lower inlet. This is only done for the stratified cases.

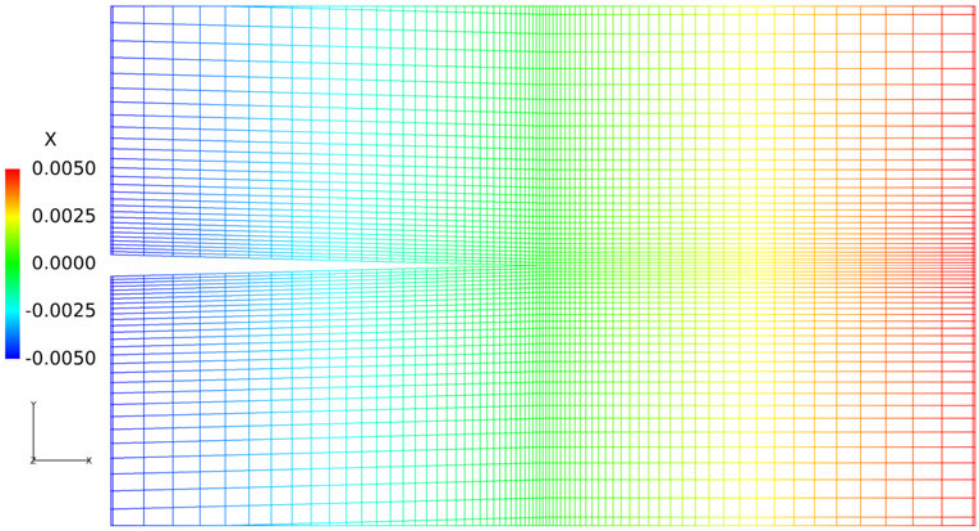

Figure 8. Close-up of the mesh around trailing edge splitter plate.

4. RESULTS

4.1. Flow dynamics of the mixing zone for LES

Vertical profiles of mean velocity $\bar{u}$ and TKE k were extracted for downstream positions $x = 40;\ 150;\ 320;\ 520$ and $720mm$. Experimental and numerical results are compared in superposition. The order of magnitude for the statistical error of the experimental data is estimated and given as an example to measurement T1, according to the theory of Bendat and Piersol [19]. Using the profile extracted at distance $x = 200mm$ past the splitter plate tip, an average velocity of $\bar{u} = 9.50m/s$ in the core of the flow with a corresponding standard deviation of $u' = 0.35m/s$ is estimated. Thus the two sided uncertainty with 95% confidence level is estimated at $\varepsilon(\bar{u}) = \pm 0.02m/s$ absolute or 0.24% relative. Since the error for the standard deviation is non-symmetric, the two sided uncertainty levels can be estimated as:

$$u' = 0.37^{+0.02}_{-0.02}\ m/s, \quad \text{absolute or} \tag{11}$$

$$\varepsilon(u') = -4.15\ \% \quad \text{and} \quad (u') = +4.53\ \%\ , \tag{12}$$

relative again with a confidence level of 95%. In case T1 isokinetic, unstratified mixing was conducted as a reference experiment to qualitatively compare the influence of stratification on the development of the mixing layer. Figure 9 shows vertical extracted profiles of stream wise mean velocity u for downstream distances $x = 40;\ 150;\ 320;\ 520$ and $720mm$. Experimental results are presented by symbols, results from the corresponding LES simulation are illustrated by lines. The nominal velocities in each leg were set both equal to $u_1 = u_2 = 8m/s$. With respect to the recorded volumetric flow rate for this experiment the corresponding nominal inlet velocities, recorded by the GAMILO, differ about 0.25%, which can be considered isokinetic. There is a fair symmetry of the velocity profile shape across the mixing layer. The developing momentum thickness on each side of the splitter plate coalesce behind the trailing edge into one profile and lead to a decay of mean velocity in the center of the mixing zone. At this position the influence of this merging already spans approximately $\approx 10 < y < 10mm$ with increasing width further downstream. Up to the end of the measurement section the wake is still present.

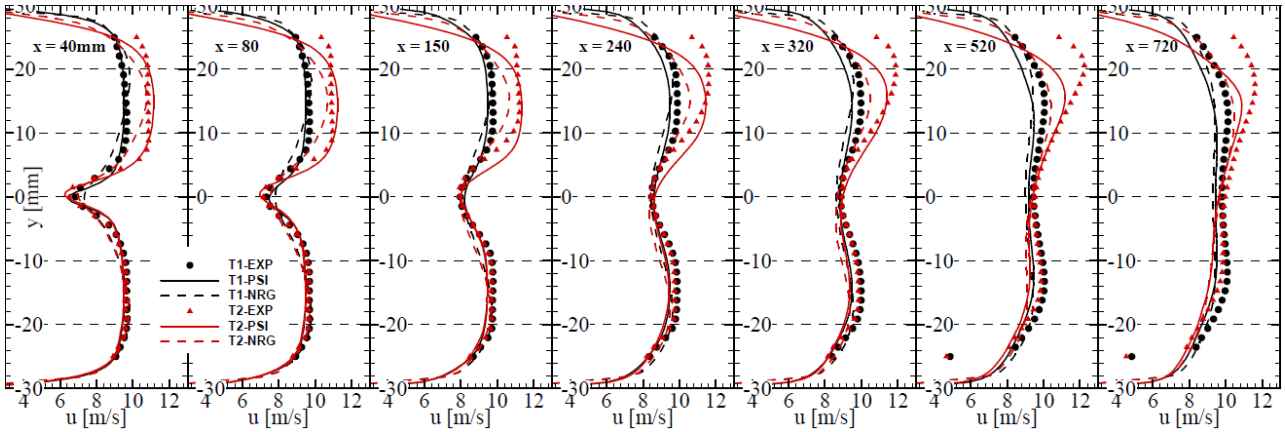

Figure 9. Vertical Profiles of streamwise mean velocity $\bar{u}$ for cases T1 and T2 (Symbols show experimental results, lines show LES results).

Downstream, approximately between $300 < x < 500mm$, the developing boundary layer of the top and bottom walls begin to interact with the wake of the mixing layer, introducing an additional influence on the developing mixing zone.

Compared to the reference experiment T1 a stronger development of the boundary layer in the upper branch, due to higher kinematic viscosity in the upper stream, is causing the core velocity to accelerate more than the core velocity of the lower stream. This effect in turn leads to the development of shear further downstream and causes a tilt of the center of the mixing zone towards the stream with higher density. For all cases, the results of LES simulation match nearly perfect at the beginning of the mixing zone $x = 40mm$. This is of course, due to the fact that the inlet conditions of the simulation were sensitively adjusted to the shape of the velocity profile at downstream position of $x = 17mm$. Overall the shape of the extracted profiles is in good agreement with experimental results, although for both cases an increasing underestimation of the mean velocity further downstream is observed. Regarding the center of the mixing zone, a minimal asymmetry is detected from LES results for case T1, which is caused by the mesh, according to the limitation of cut-cell method to reproduce the exact shape of a sharp edge of the splitter plate. The effect is also contributing to the fluctuating quantities of the flow field, which can be seen in Fig. 10, where vertical profiles of TKE are plotted.

Although the core flow velocities of the helium stream in the high stratified experiment T2 are higher compared to the nitrogen stream and the flow is considered in the transition from laminar to turbulent regime, the velocity profile at the inlet of the measurement section match fairly well with simulation results. The mixing layer, the core flow and the momentum thickness of the nitrogen leg match perfectly, while in the helium leg, the measured boundary layer at the top wall differs significantly from the LES results. The effect of the grids in the flow conditioning becomes more striking for this case, due to the high kinematic viscous helium stream, and the difference evolves further downstream. Despite this particular discrepancy between measured and simulated results, the shape and magnitude match very well.

4.1.1. Turbulent Kinetic Energy

For the calculation of TKE from LES simulations, all three fluctuating components of the vector field are used, since the z-component is available. A comparison of both methods in calculating the TKE revealed almost no difference, and the contribution of the streamwise fluctuating part is dominating both perpendicular components. At position $x = 40mm$ a turbulent intensity of about 3.5% is measured in the

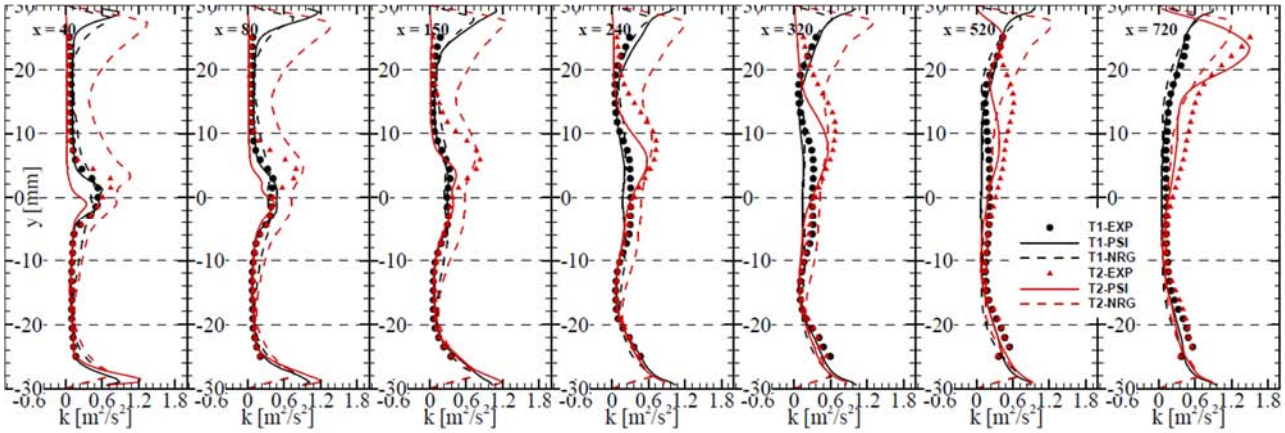

Figure 10. Vertical Profiles of TKE for cases T1 and T2 (Symbols show experimental results, lines show LES results).

core of both streams for both cases. Figures 10 shows vertically extracted profiles of TKE for experiments T1 and T2, respectively. High turbulent intensities in the boundary layers are observed for both cases at this location which are developing downstream. However the turbulent intensity at the beginning of the mixing zone is much larger in magnitude, compared to the simulation. For the unstratified experiment T1 the development of TKE is almost symmetric on both sides of the mixing zone, while the development of the boundary layer in the upper leg, with less dense gas, is introducing more TKE to the flow, compared to the lower leg. The same effect is visible in the development of the mixing layer, where an asymmetric distribution of TKE development is detected for the stratified case. A transport of TKE from the high dense stream across the mixing layer towards the less dense stream is observed. The simulated development of TKE is over predicting the TKE in the less denser boundary layer but in turn under predicting the high density side. For the high stratified case T2, the under prediction in transport of TKE is significant and sustains towards the whole mixing layer. The difference in magnitude of the peak in the center of the mixing zone right behind the trailing edge can be explained by their different geometry. A transport in momentum could possibly cause high vertical fluctuations of velocity in the vicinity of the less dense, highly viscous part of the mixing zone and increases the extend of mixing, instead of damping due to stable density stratification.

A strong production of TKE is observed in the near wall region right at the inlet to the measurement section and developing further downstream. This effect indicates an already turbulent boundary layer for the reference experiment. For the stratified case T2 the boundary layer in the lower branch is found to be turbulent but on the upper branch, the initially laminar boundary layer undergoes the transition from laminar to turbulent further downstream between 300 < x < 500mm. However a strong production of TKE is observed on the upper side of the developing mixing layer, which is growing downstream into the less dense, high viscous side. The assumption of a fully developed turbulent flow in the helium leg for high stratified case T2 shows significant difference in mean velocity and for TKE this difference is even more striking. The merging of both boundary layers at the trailing edge of the splitter plate yields to an over prediction of turbulence in the upper leg and as expected, much higher turbulence level for the simulated case with respect to the boundary layer of the top wall.

4.1.2. Normal components of the Reynolds stress tensor

Normal components of the Reynolds stress tensor τ_{xx} are shown in Fig. 11. The vertical components τ_{yy} are shown in Fig. 12. According to boundary layer theory [17], velocity fluctuations in the near wall region increase with increasing downstream distance. This effect has its origin in the formation of shear due to the influence of viscous forces from the wall acting on fluid elements. For the reference case T1, a strong development of velocity fluctuations is observed in the mixing zone. A minimum of streamwise

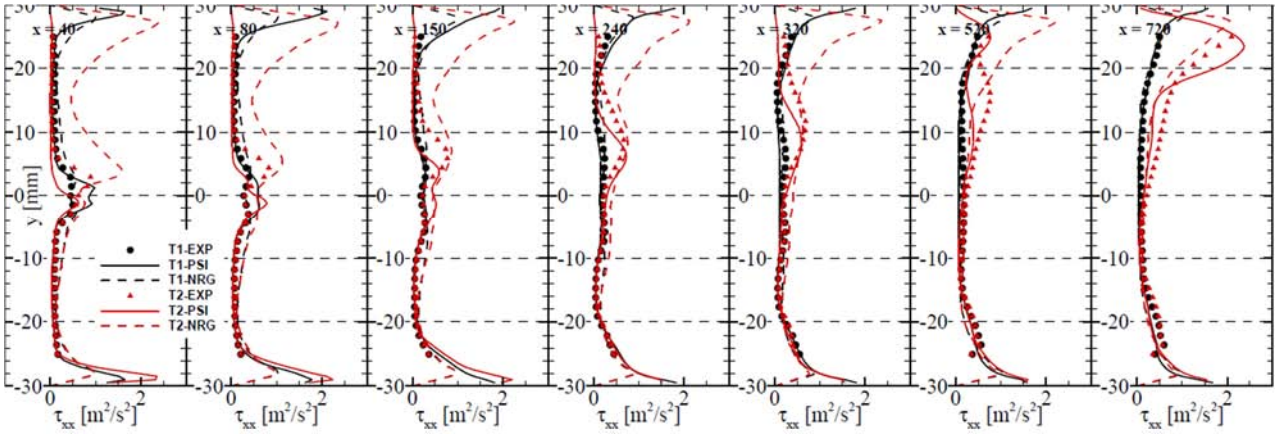

Figure 11. Normal components of the Reynolds stress tensor τ_{xx} for cases T1 and T2 (Symbols show experimental results, lines show LES results).

fluctuations in conjunction with a peak in the perpendicular fluctuations indicate the formation of paired rollers, forming on each side of the mixing zone. For case T2 the downstream development of fluctuations in the mixing zone is even higher and achieves a maximum peak between $300 < x < 500mm$. In this stage the developing boundary layer of the upper leg merges with the mixing layer and viscous forces affect the whole upper branch.

Compared to the measured streamwise velocity fluctuations, the resulting fluctuations of LES from PSI predict the statistics fairly well in shape. The magnitude of fluctuations in the core of each side, is however under predicted, while the difference on the top wall side might be caused by the grid configuration in the experiment, since the profiles are in good agreement on the bottom side and towards the end of the whole test section. This is different for the perpendicular fluctuations v'. For case T1 only the core flows on each side are well predicted. Both boundary layers are underpredicted, while for streamwise fluctuations in the wall effected regions, an over prediction is observed. These two discrepancies compensate in calculation of TKE. Both components under predict the measured fluctuation level in the mixing zone. For stratified experiment T2 high fluctuations are generated on the upper side of the mixing layer, that are spreading into the upper branch until they merge with the boundary layer. The resulting fluctuations of LES simulations performed by NRG are in very good agreement for cases T1, whereas for the high stratified case, both streamwise and perpendicular velocity fluctuations are matching the peak of the mixing layer fairly well, despite the large over prediction in the upper wall region, due to fully developed turbulence.

4.1.3. Shear stress

Figure 13 shows vertical extracted profiles of the shear stress τ_{xy}. The influence of viscous forces in the near wall region is introducing shear to the flow, which indicates the downstream development of the momentum thickness. With respect to this effect and the merging of two developed boundary layers at the tip of the splitter plate, the flow is characterized as a wake flow rather than a pure mixing layer. The span of shear within the wake is vertically growing further downstream, as velocity gradients and thus viscous forces, spread into the core flows until the core in each branch is completely infused by viscous forces contributing from the boundary layers and the mixing layer. The shear stress computed by LES agrees remarkably well with experimental results.

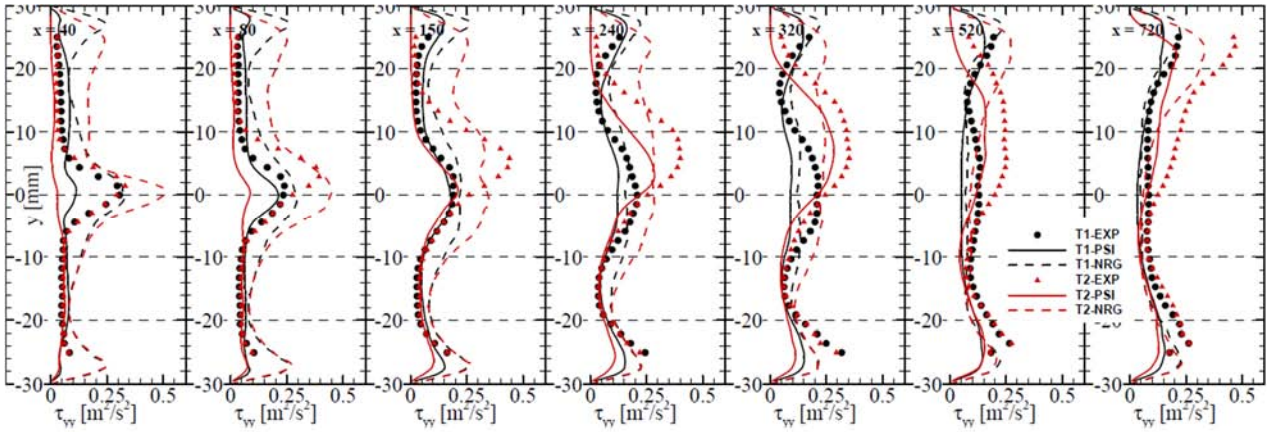

Figure 12. Normal components of the Reynolds stress tensor τ_{yy} for cases T1 and T2 (Symbols show experimental results, lines show LES results).

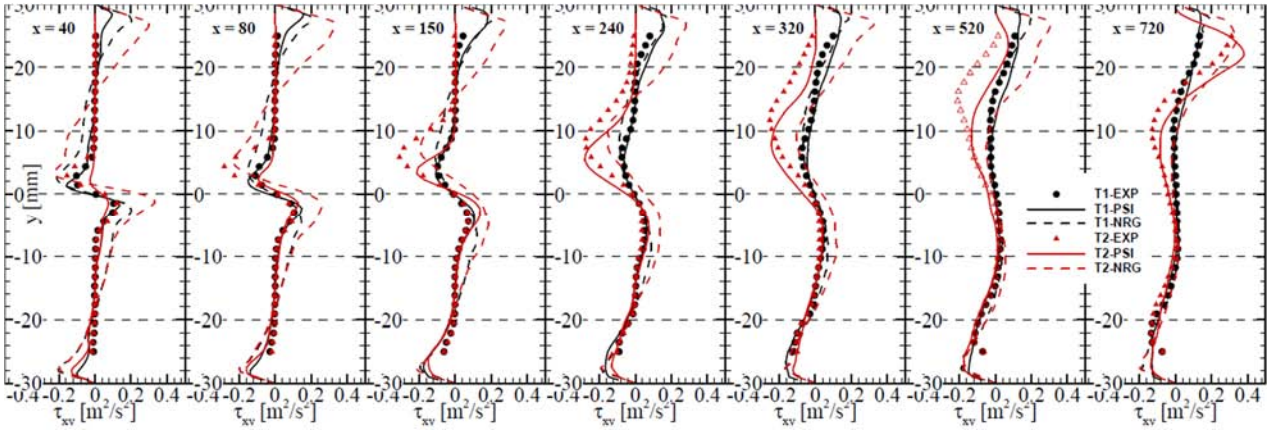

Figure 13. The shear stress τ_{xy} for cases T1 and T2 (Symbols show experimental results, lines show LES results).

5. CONCLUSIONS

Two dimensional PIV was used to record the flow field in the vertical mid-plane of a planar horizontal mixing layer. Isokinetic experiments were performed with Atwood numbers of $A = 0.0$ and -0.75. In addition a numerical investigation making use of LES methods was carried out and the resulting flow fields were quantitatively compared. Two different approaches were followed, where a partially developed flow inlet condition shows remarkably better results compared to fully developed turbulence inlet conditions. We observe a transport of TKE across the developing mixing layer from the more dense side towards the less dense side for the stratified case. The mixing layer evolves asymmetric and high production of TKE on the helium side due to the formation of shear is dominating the damping effect of buoyancy for stable stratification. The results from LES simulation are in very good agreement to the experimental results.

ACKNOWLEDGMENTS

It is a pleasure to acknowledge the considerable help which has been given by Dr. Ralf Kapulla and Dipl.-Ing. Wilhem-Martin Bissels in designing and building the HOMER facility. I am indebted to Dr. Arnoldo Badillo and Dr. Medhat Sharabi for many fruitful discussions and several helpful comments. Besides the

financial support of the THINS project within the Seventh Framework Programme of EURATOM (FP7) for nuclear Research and Training Activities (2007-2011), the work was made possible by the generous support of Swiss National Fund within grant No. 200021 141025/1. The simulations provided by the NRG were performed Swierk Computing Centre in a framework of the EU and MSHE grant no. POIG.02.03.00-00-013/09.

REFERENCES

[1] ABARZHI, S.I. (2010) Review of theoretical modelling approaches of Rayleigh -Taylor instabilities and turbulent mixing Philosophical Transactions of the Royal Society A, 368, 1809–1828

[2] TAILLEUX, R.G.J. (2009) On the energetics of stratified turbulent mixing, irreversible thermodynamics, Boussinesq models and the ocean heat engine controversy Journal of Fluid Mechanics, 638, 339-382

[3] ZILITINKEVICH, S.S. et.al. (2008) Turbulence energetics in stably stratified geophysical flows: Strong and weak mixing regimes Quarterly Journal of the Royal Meteorological Society, 134, 793-799

[4] THORPE, S.A. (2007) An Introduction to Ocean Turbulence ISBN 978-0-521-85948-6, Cambridge University Press

[5] ANSELMO-FILHO, P. et.al. (2009) Experimental measurements of geometric properties of turbulent stratified flames Proceedings of the Combustion Institute, 32, Issue 2, 1763-1770

[6] ROBIN, V. et.al. (2008) Experimental and numerical analysis of stratified turbulent V-shaped flames Combustion and Flame, 153, Issue 12, 288-315

[7] DRISCOLL, J.F. (2008) Turbulent premixed combustion: Flamelet structure and its effect on turbulent burning velocities. Progress in Energy and Combustion Science, 34, Issue 1, 91-134.

[8] CARRE, F. et.al. (2010) Update of the French R&D strategy on gas-cooled reactors. Nuclear Engineering and Design, 240, 2401–2408.

[9] ANSYS FLUENT 14.5 (2012) Theory Guide ANSYS, Inc.

[10] MENTER, F.R. (1993) Zonal two-equation k-! turbulence models for aerodynamic flows AIAA Journal, 93.

[11] Van LEER, B. (1979) Towards the ultimate conservative scheme. IV. A second order sequel to Godunovs method Journal of Computational Physics, 32, 101–136.

[12] VANDOORMAAL, J.P. and RAITHBY, G.D. (1984) Enhancements of the SIMPLE method for predicting incompressible fluid flows Numerical Heat Transfer, 7, 147–163.

[13] NICOUD, F. and DUCROS, F. (1999) Subgrid-scale modeling based on the square of the velocity gradient tensor Flow, Turbulence and Combusion, 62, 183–200

[14] www.openfoam.org

[15] PRONO, L. and SMAGORINSKY, J. (2008) In S. Philander (Ed.) Encyclopedia of global warming and climate change, Thousand Oaks, CA: SAGE Publications, Inc. 903–904

[16] ZHAO, H. and VOKE, P.R. (1998) A DYNAMIC SUBGRID-SCALE MODEL FOR LOW-REYNOLDS-NUMBER CHANNEL FLOW Numerical Methods in Fluids.

[17] SCHLICHTING, H. (1979) Boundary-Layer Theory McGraw-Hill Book Company.

[18] LEMMON, E. and HUBER, M. and MCLINDEN, M. (2010). NIST Standard Reference Database 23: Reference Fluid Thermodynamic and Transport Properties-REFPROP, Version 9.0. National Institute of Standards and Technology, Standard Reference Data Program.

[19] BENDAT, J.S. and PIERSOL, A.G. (2011). Random Data: Analysis and Measurement Procedures. John Wiley & Sons.

[20] LaVision (2014). Product Manual for DaVis 8.2. LaVision GmbH, Germany.